1

2

3

4

A Modified Method for Inferring Upper Cloud Top Height Using the GOES-12 Imager 10.7- and 13.3-μm Data

7

8

Fu-Lung Chang[1], Patrick Minnis[2], Bing Lin[2], Mandana Khaiyer[3], Rabindra Palikonda[3], and Douglas Spangenberg[3]

11

12

(1) National Institute of Aerospace, Hampton, Virginia

(2) NASA Langley Research Center, Hampton, Virginia

(3) Science Systems and Applications Inc., Hampton, Virginia

16

17

18

19

Corresponding author address:

Dr. Fu-Lung Chang

Mail Stop 420, NASA Langley Research Center, Hampton, Virginia 23681

Email: Fu-Lung.Chang-1@nasa.gov

24

Abstract

Accurate inference of upper transmissive cloud top height (CTH) is often difficult using passive meteorological satellite instruments. Satellite retrievals using conventional CO_2-slicing or CO_2-absorption techniques tend to systematically underestimate the upper CTHs. These techniques are based on single-layer assumptions that the upper cloud occupies a geometrically thin layer above a cloud-free surface. This study presents a new modified CO_2-absorption technique (MCO2AT) to improve the inference of upper CTH. The MCO2AT consists of three steps starting with a single-layer CO_2-absorption technique (SCO2AT) followed by iterative retrieval procedures to obtain an enhanced upper CTH based on inferred effective background radiances. The MCO2AT is applied to one-month of half-hourly Geostationary Operational Environmental Satellite (GOES) imager 10.7- and 13.3-μm data. Both the MCO2AT- and SCO2AT-inferred upper CTHs are compared with those obtained from the ground-based Active Remotely Sensed Cloud Location (ARSCL) dataset taken at the Atmospheric Radiation Measurement (ARM) Southern Great Plains Central Facility. For overcast upper-cloud scenes, the mean upper CTH differences are −0.33 (±1.54) km for MCO2AT minus ARSCL in contrast to −1.58 (±2.08) km for SCO2AT minus ARSCL. For broken upper-cloud scenes, the respective corresponding differences are −2.66 (±1.80) km and −4.73 (±2.28) km. Overall, the MCO2AT worked more effectively on multilayer clouds and optically thin, geometrically thick clouds. The comparisons also revealed that more than 10% of the upper thin cirrus cases detected by the ARSCL were not retrieved by the MCO2AT and SCO2AT, suggesting that a more sensitive cirrus cloud retrieval algorithm is needed.

1. Introduction

To infer upper cloud top height (CTH), current meteorological satellites usually employ a window technique that is based on analyses of the infrared (IR) and visible radiances obtained at atmospheric window channels [e.g., Rossow and Schiffer, 1991, 1999; Minnis et al., 1993, 2009] or a CO_2-slicing technique that is based on analyses of a suit of the multispectral IR sounding radiances obtained at various carbon dioxide (CO_2) absorption channels having nominal wavelengths of 13.3, 13.6, 13.9 and 14.3 μm [e.g., Chahine, 1974; McCleese and Wilson, 1976; Smith and Platt, 1978; Menzel et al., 1983, 1992; Smith and Frey, 1990]. Standard window techniques tend to underestimate the occurrence of highly transmissive cirrus clouds [Rossow, 1989; Wylie and Menzel, 1989, 1999; Jin et al., 1996]. Many of those missed clouds can be detected using the CO_2-slicing technique, which exploits the multiple IR sounding channels, with their varying spectral absorptivities and sensitivities, to infer the cloud-top pressure (CTP) and, hence, the CTH.

Window techniques have typically been used to analyze 4-km data from the imagers on Geostationary Operational Environmental Satellite (GOES) I series, GOES-8 through GOES-11 [e.g., Smith et al., 2008], which measure radiances at five nominal wavelengths, 0.65, 3.9, 6.7, 10.7 and 12 μm [Menzel and Purdom, 1994]. The CO_2-slicing technique, on the other hand, has generally been applied to the relatively low spatial resolution (~12 km) GOES sounder data, which are taken at one visible and several IR channels including various CO_2-absorption bands [Menzel and Purdom, 1994; Schreiner et al., 2001]. However, beginning with GOES-12, the GOES-I imagers have a new 13.3-μm channel in place of the 12-μm channel. This channel modification was made to improve the cloud products derived from the GOES-I imagers [Schmit et al., 2001].

2

70   To that end, this study explores a new modified CO_2-absorption technique that

71   employs the limited 10.7- and 13.3-μm channel pair for improving the inference of upper

72   CTH. It has been shown that the performance of a CO_2-slicing technique depends on the

73   channels used; different channel selections can result in different CTH solutions [Wielicki and

74   Coakley, 1981; Eyre and Menzel, 1989]. In their theoretical study, Wielicki and Coakley

75   [1981] noted that using the lower-wavelength sounding channels, which have the least

76   atmospheric absorption, would retrieve the majority clouds throughout the troposphere. The

77   higher sounding channels, which are more absorbing, would be limited mostly to detecting

78   high clouds due to increased atmospheric opacity and reduced signal-to-noise ratios.

79   However, it was also noted that the retrieval skill using the lower sounding channels would be

80   degraded when the clear-sky radiances have significant uncertainties. While the uncertainties

81   in clear-sky radiances generally imply the assumption of a single cloud layer, in more

82   complex multilayer clouds the uncertainties also imply the impact by the presence of lower

83   clouds underneath an upper cloud. In multilayer cases, the upwelling background radiances

84   are no longer represented by the clear-sky radiances and the assumption of single-layer cloud

85   can cause underestimations in the upper cloud CTHs [e.g., Chang and Li, 2005].

86   Among past validation studies, Wylie and Menzel [1989] compared the CO_2-slicing

87   CTPs derived using the GOES VISSR Atmospheric Sounder (VAS) data to those derived

88   from the ground-based lidar data, radiosonde moisture profiles, and GOES parallax

89   measurements. Their results, which excluded multilayer and broken clouds, optically thin

90   cirrus, and low-level stratocumulus, show that the averaged VAS-derived CTPs were within

91   approximately ±50 hPa of the other CTP measurements. Frey et al. [1999] compared the

92   CO_2-slicing CTHs derived using the Moderate-resolution Imaging Spectroradiometer

93   (MODIS) Airborne Simulator (MAS) data to collocated airborne lidar data and found that the

94   two CTHs agreed to within ±0.5 km for 32% and within ±1.5 km for 64% of the cases studied.

95   Schreiner et al. [2001] compared CO_2-slicing CTHs derived from GOES-8 sounder data to the

96   altitudes of apparent single-layer clouds estimated by Pilot Reports (PIREPs). They found

97   that for high clouds the GOES-8 CTHs were, on average, ~910 m lower than the PIREPs data.

98   Hawkinson et al. [2005] compared GOES-8 sounder CO_2-slicing retrievals of CTH to the

99   ground-based Active Remotely Sensed Cloud Location (ARSCL) products [Clothiaux et al.,

100   2000] of the Atmospheric Radiation Measurement (ARM) Program [Ackerman and Stokes,

101   2003], but they only used cases having relatively uniform GOES-8 CTHs. They found that

102   the GOES-8 CTHs were lower than the ARSCL cloud tops by an average of 1.8 km with a

103   standard deviation of 1.7 km.

104   More recently, Holz et al. [2006] evaluated the optically thin cirrus cases having a

105   total optical depth less than 1 by comparing CTHs inferred from MAS data to collocated

106   airborne Cloud Physics Lidar (CPL) data. They reported that for geometrically thick but

107   optically thin clouds, the CO_2-slicing CTHs were underestimated by more than 3 km. They

108   suggest that the bias in CTH could be reduced using the hyper-spectral Scanning High-

109   resolution Interferometer Sounder (S-HIS) measurements. Bedka et al. [2007] compared the

110   GOES-12 sounder and imager data but studied only two cloud cases, one consisting of clouds

111   at different levels and the other consisting entirely of single mid-level clouds obtained during

112   the Atlantic-THORPEX Regional Campaign (ATReC). Comparisons with averaged airborne-

113   CPL data show that for high clouds above 10 km, the CPL minus the GOES-12 sounder and

114   imager CTHs yield mean biases of ~3.8 km $\pm$ 2.9 km) and ~3.1 km $\pm$ 2.7 km, respectively.

115   For the other mid-level clouds, the mean biases were slightly less than 1 km (rms ~1 km). In

4

116   comparisons with ARSCL data, Smith et al. [2008] found results similar to Hawkinson et al.

117   [2005] using GOES-8 sounder retrievals of CTH for all single-layer clouds. However, for

118   cirrus clouds having optical depths less than 3, the CO_2-slicing results produced an average

119   underestimate of 2.9 km $\pm$ 2.0 km.

120   This study presents a new modified CO_2-absorbing technique aimed at improving on

121   some of the common assumptions used in conventional single-layer CO_2-slicing techniques.

122   The targeted assumptions are 1) the cloud occupies a single layer in the field of view (FOV)

123   of the satellite instrument, 2) the single-layer cloud occupies infinitesimal or zero thickness by

124   neglecting the cloud geometric thickness effect, 3) the emissivity of the cloud is the same in

125   all sounding channels, and 4) the emissivity of the clear-sky surface is unity. Since

126   conventional single-layer CO_2-slicing techniques systematically underestimate upper CTHs,

127   the primary objectives of the modified CO_2-absorbing technique are: 1) to remedy the

128   underestimation of upper cirrus CTH caused by the potential impact of underlying lower

129   cloud, 2) to remedy the underestimation of single-layer cirrus CTH caused by the assumption

130   of an infinitesimal thin cloud thickness, 3) to enhance the retrieval skill by reducing the

131   impact of the uncertainties in surface emissivities and clear-sky radiances, and 4) to enhance

132   the retrieval skill by relating the spectral cloud emissivities at the 10.7- and 13.3-μm channels.

133   In Section 2, our new modified CO_2-absorbing technique is delineated following a

134   brief review of the conventional single-layer CO_2-slicing technique. Section 3 describes the

135   data sets used herein. Section 4 presents comparisons of the results obtained from the

136   conventional single-layer and our modified CO_2-absorbing techniques and examines those

137   comparisons relative to the ground-based ARM ARSCL data. Section 5 gives the concluding

138   remarks.

139

2. Techniques

2.1. Single-layer CO$_2$-absorption Technique

There are a handful of references on the CO$_2$-slicing or CO$_2$-absorption retrieval

technique (see previous section). Since all operational CO$_2$-absorption techniques are based

on a single-layer cloud assumption, hereafter, this method is referred to as the single-layer

CO$_2$-absorption technique (SCO2AT). We briefly describe the SCO2AT that utilizes the

radiance pair obtained by the GOES-12 imager: 10.7-μm (hereafter channel 4) and 13.3-μm

channel (hereafter channel 6). [Note that the 12.0-μm channel is nominally channel 5, c.f.

Schmit et al., 2001].

Let us begin by considering a cloud-free pixel. The satellite-observed clear-sky

radiance R_{clr}^{λ} at a spectral channel λ is given by

$$R_{clr}^{\lambda} = B^{\lambda}(T_g)\xi^{\lambda}(P_g) + \int_{P_g}^{0} B^{\lambda}(T(P)) \frac{d\xi^{\lambda}(P)}{d\ln P} d\ln P , \qquad (1)$$

where $B^{\lambda}(T)$ denotes the Planck radiance at channel λ and temperature T, $\xi^{\lambda}(P)$ denotes

the transmittance between atmospheric pressure level P and $P = 0$ (at the imager level), and

the subscript g denotes the ground surface level. In (1), it is assumed that the surface

emissivity = 1. Similarly, the opaque-cloud radiance R_{ovc}^{λ} observed for a completely overcast

pixel at channel λ is given by

$$R_{ovc}^{\lambda} = B^{\lambda}(T_c)\xi^{\lambda}(P_c) + \int_{P_c}^{0} B^{\lambda}(T(P)) \frac{d\xi^{\lambda}(P)}{d\ln P} d\ln P , \qquad (2)$$

where the subscript c denotes the cloud top level.

6

159   In the CO$_2$-IR channels, cloud reflectivity is assumed to be negligible and, thus, cloud

160   transmissivity t_c^λ can be related to cloud emissivity e_c^λ by $t_c^\lambda = 1 - e_c^\lambda$. As such, the spectral

161   radiance R_{pix}^λ for a cloudy pixel is given by

$$R_{pix}^\lambda = \varepsilon_c^\lambda R_{ovc}^\lambda + (1 - \varepsilon_c^\lambda) R_{clr}^\lambda, \tag{3}$$

163   where $\varepsilon_c^\lambda = e_c^\lambda A_c$ is an effective cloud emissivity with A_c being the cloud cover fraction of

164   the pixel. As a result, for opaque clouds (i.e., $e_c^\lambda = 1$), ε_c^λ is equivalent to the fractional

165   coverage of the opaque cloud (i.e., A_c) and for completely overcast pixels (i.e., $A_c = 1$), ε_c^λ is

166   equivalent to the emissivity of the overcast cloud (i.e., e_c^λ).

167   Let us use the superscripts Ch4 and Ch6 for the 10.7-μm and 13.3-μm channels,

168   respectively, and write (3) separately for the two channels as

$$R_{pix}^{Ch4} = \varepsilon_c^{Ch4} R_{ovc}^{Ch4} + (1 - \varepsilon_c^{Ch4}) R_{clr}^{Ch4} \tag{4}$$

$$R_{pix}^{Ch6} = \varepsilon_c^{Ch6} R_{ovc}^{Ch6} + (1 - \varepsilon_c^{Ch6}) R_{clr}^{Ch6}. \tag{5}$$

171   We can manipulate (4) and (5) to derive the ratios of the two channels for the cloud radiative

172   effects to yield

$$\frac{R_{pix}^{Ch6} - R_{clr}^{Ch6}}{R_{pix}^{Ch4} - R_{clr}^{Ch4}} = \frac{\varepsilon_c^{Ch6}(R_{ovc}^{Ch6} - R_{clr}^{Ch6})}{\varepsilon_c^{Ch4}(R_{ovc}^{Ch4} - R_{clr}^{Ch4})}. \tag{6}$$

174   This two-channel approach obtained in (6) has been referred to as the radiance ratioing

175   method in previous studies [Wielicki and Coakley, 1981; Eyre and Menzel, 1989].

176   Previous applications of the radiance ratioing method in (6) assume that the spectral

177   cloud emissivities at two different channels are the same (i.e., $\varepsilon_c^{Ch4} = \varepsilon_c^{Ch6}$). This assumption

178   requires the two channels to be spectrally close. To infer the CTH, the left-hand side of (6)

179   represents the satellite-observed cloud radiative difference ratio (i.e., R_{pix}^{Ch4} and R_{pix}^{Ch6}) and the

180   right-hand side of (6) represents the same ratio estimated using radiative transfer calculations

181   (i.e., R_{ovc}^{Ch4} and R_{ovc}^{Ch6}). In practice, solution of the inferred CTH for a cloudy pixel is obtained

182   by finding the optimal values of P_c and T_c that best satisfy (6) with a minimum difference

183   between the two sides of the equation.

184   As seen in (6), however, the SCO2AT invokes the assumption of clear-sky

185   background radiances (i.e., R_{clr}^{Ch4} and R_{clr}^{Ch6}). Since clear-sky radiances can not be directly

186   observed in a cloudy pixel, they have to be obtained either from simulations based on

187   radiative transfer calculations or from interpolations based on other cloud-free candidates

188   found elsewhere. To this end, simulations based on radiative transfer calculations often serve

189   as a better means because synoptic clouds in nature often extend over a large geographic area

190   and for a long period of time, which hampers the measurement of nearby clear-sky radiances.

191   The input data required for the radiative transfer calculations, atmospheric temperature and

192   moisture profiles and surface temperatures and emissivities, are usually based on numerical

193   weather analyses or forecasts. Nevertheless, Eq. (6) is not appropriate for a multilayer cloud

194   situation.

195

196   **2.2. Modified CO_2-absorption Technique**

197   The modified CO_2-absorption technique (MCO2AT) is proposed to use inferred

198   effective background radiances to replace the clear-sky radiances. In an idealized two-layer

199   cloud situation, the effective background radiances represent the blackbody lower-cloud

200   radiances. In reality, the effective background radiances are often a mixture of clear-sky

201   radiances and/or lower-cloud radiances in single-layer and multilayer cloud situations.

202   Here let us consider an imager pixel containing two idealized cloud layers. We

203   assume that the lower cloud layer can be represented by a slab of opaque cloud at an effective

204   background level defined by the pressure P_{ebg} and temperature T_{ebg}, where the subscript *ebg*

205   denotes the effective background. Following Eqs. (1) and (2) in the previous section, the

206   effective background radiances R_{ebg}^{Ch4} and R_{ebg}^{Ch6} for channels 4 and 6, respectively, are given

207   by

208
$$R_{ebg}^{Ch4} = B^{Ch4}(T_{ebg})\xi^{Ch4}(P_{ebg}) + \int_{P_{ebg}}^{0} B^{Ch4}(T(P))\frac{d\xi^{Ch4}(P)}{d\ln P}d\ln P \qquad (7)$$

209
$$R_{ebg}^{Ch6} = B^{Ch6}(T_{ebg})\xi^{Ch6}(P_{ebg}) + \int_{P_{ebg}}^{0} B^{Ch6}(T(P))\frac{d\xi^{Ch6}(P)}{d\ln P}d\ln P \qquad (8)$$

210   Then following equations (4)-(6), we obtain a new set of equations (9)-(11):

211
$$R_{pix}^{Ch4} = \varepsilon_c^{Ch4}R_{ovc}^{Ch4} + (1-\varepsilon_c^{Ch4})R_{ebg}^{Ch4}, \qquad (9)$$

212
$$R_{pix}^{Ch6} = \varepsilon_c^{Ch6}R_{ovc}^{Ch6} + (1-\varepsilon_c^{Ch6})R_{ebg}^{Ch6}, \qquad (10)$$

213   and

214
$$\frac{R_{pix}^{Ch6} - R_{ebg}^{Ch6}}{R_{pix}^{Ch4} - R_{ebg}^{Ch4}} = \frac{\varepsilon_c^{Ch6}(R_{ovc}^{Ch6} - R_{ebg}^{Ch6})}{\varepsilon_c^{Ch4}(R_{ovc}^{Ch4} - R_{ebg}^{Ch4})}. \qquad (11)$$

215   For different spectral cloud emissivities, we can relate ε_c^{Ch4} and ε_c^{Ch6} by

216
$$\frac{\varepsilon_c^{Ch6}}{\varepsilon_c^{Ch4}} = \frac{1-\exp(-\tau_c^{Ch6}/\mu)}{1-\exp(-\tau_c^{Ch4}/\mu)}, \qquad (12)$$

217   and

218
$$\frac{\tau_c^{Ch6}}{\tau_c^{Ch4}} = \frac{\sigma_{ext}^{Ch6}}{\sigma_{ext}^{Ch4}}, \qquad (13)$$

219 where τ_c^{Ch4} and τ_c^{Ch6} denote the corresponding spectral cloud optical depths, $\sigma_{ext}^{\text{Ch4}}$ and $\sigma_{ext}^{\text{Ch6}}$

220 denote the corresponding spectral extinction coefficients, and μ denotes the cosine of

221 satellite viewing zenith angle.

222   The modified Eq. (11) invokes the assumption of effective background radiances,

223 R_{ebg}^{Ch4} and R_{ebg}^{Ch6}, which replace their counterparts in (6), the clear-sky radiances, R_{clr}^{Ch4} and

224 R_{clr}^{Ch6}. The effective background radiances also can not be directly observed because the

225 upper cloud layer obscures the imager FOV. In practice, for the pixel-retrieval applications,

226 we have developed an iterative retrieval procedure that applies the MCO2AT to infer

227 alternatively the effective background radiances and enhanced overcast radiances, R_{ovc}^{Ch4} and

228 R_{ovc}^{Ch6}, from which the effective background level $[P_{ebg}, T_{ebg}]$ and the improved upper CTH

229 $[P_c, T_c]$ can be obtained. The iterative retrieval procedure consists of three main steps as

230 described below. Step 1 basically applies the SCO2AT. If the SCO2AT retrieval in the first

231 step is successful, the second step determines if the MCO2AT should be applied. The third

232 step is then the essential component of the MCO2AT. The components of each step are listed

233 sequentially as follows.

234   1A. Initialize the effective background level at the ground level, i.e., $[P_{ebg}, T_{ebg}] = [P_g, T_g]$.

235   1B. Infer the clear-sky radiances R_{clr}^{Ch4} and R_{clr}^{Ch6} using Eq. (1).

236   1C. Retrieve an optimal solution set $[P_c, T_c]$ and R_{ovc}^{Ch4} and R_{ovc}^{Ch6}, which best satisfies Eq.

237   (6) using the single-layer assumption.

238   1D. If $P_c > 600$ hPa or $P_c > (P_g - 300\text{hPa})$, go to Step 4C;

239   Otherwise, proceed to Step 2A.

240   2A. Initialize $R_{ebg}^{\text{Ch4}} = R_{pix}^{\text{Ch4}}$ and use Eq. (7) to retrieve a rough solution set $[P_{ebg}, T_{ebg}]$.

241   2B. Use the rough solution set $[P_{ebg}, T_{ebg}]$ and Eq. (8) to infer a rough R_{ebg}^{Ch6}.

242   2C. Compare the observed R_{pix}^{Ch6} with the rough R_{ebg}^{Ch6}.

243   2D. If $R_{pix}^{\text{Ch6}} - R_{ebg}^{\text{Ch6}} > -\delta_R^{\text{Ch6}}$, go to Step 4B (here, δ_R^{Ch6} is the 13.3-μm noise level);

244   Otherwise, proceed to Step 3A.

245   3A. Take $[P_c, T_c]$ from Step 1C and take R_{ebg}^{Ch6} from Step 2B.

246   3B. Use $[P_c, T_c]$ and Eq. (2) for Channel 6 to infer R_{ovc}^{Ch6}, and then obtain $\varepsilon_c^{\text{Ch6}} =$

247          $(R_{pix}^{\text{Ch6}} - R_{ebg}^{\text{Ch6}})/(R_{ovc}^{\text{Ch6}} - R_{ebg}^{\text{Ch6}})$ from Eq. (10).

248   3C. Obtain $\varepsilon_c^{\text{Ch4}}$ through $\varepsilon_c^{\text{Ch6}}$ using Eqs. (11) and (12).

249   3D. Use $[P_c, T_c]$ and Eq. (2) for Channel 4 to infer R_{ovc}^{Ch4}, and then obtain $R_{ebg}^{\text{Ch4}} =$

250          $(R_{pix}^{\text{Ch4}} - \varepsilon_c^{\text{Ch4}} R_{ovc}^{\text{Ch4}})/(1 - \varepsilon_c^{\text{Ch4}})$ from Eq. (9). Here, R_{ebg}^{Ch4} is bounded by a maximum at

251          $R_{ebg}^{\text{Ch4}} = R_{clr}^{\text{Ch4}}$ and by a minimum at $R_{ebg}^{\text{Ch4}} = (R_{clr}^{\text{Ch4}} + R_{ovc}^{\text{Ch4}})/2$.

252   3E. Use the new R_{ebg}^{Ch4} and Eq. (7) to retrieve a new solution set $[P_{ebg}, T_{ebg}]$.

253   3F. Use the new solution set $[P_{ebg}, T_{ebg}]$ and Eq. (8) to infer new R_{ebg}^{Ch6}.

254   3G. Retrieve the optimal solution set $[P_c, T_c]$ and R_{ovc}^{Ch4} and R_{ovc}^{Ch6}, which best satisfies Eq.

255   (11) in the modified method.

256   3H. If $\left| \text{new } R_{ebg}^{\text{Ch6}} - \text{old } R_{ebg}^{\text{Ch6}} \right| > \delta_R^{\text{Ch6}}$, repeat Steps 3B-3H; Otherwise, go to Step 4A.

257   4A. The solution set $[P_c, T_c]$ is retrieved from the MCO2AT with $[P_{ebg}, T_{ebg}]$. Stop.

258   4B. The solution set $[P_c, T_c]$ is retrieved from the SCO2AT with $[P_{ebg}, T_{ebg}] = [P_g, T_g]$.

259   Stop.

260   4C.   No upper cloud (i.e., no $P_c < 600$ hPa) is retrieved. Stop.

261   The above retrieval steps will give a cloud pixel a possible upper CTH solution set

262    $[P_c, T_c]$ inferred by the MCO2AT (4A) for an enhanced CO_2-CTH or by the SCO2AT (4B)

263   for a regular CO_2-CTH. The upper CTH is inferred by finding the altitude corresponding to P_c

264   in an appropriate vertical profile of pressure levels. The threshold of 600 hPa (~4.3 km) is

265   selected conservatively because the CO_2-absorption method becomes less certain towards

266   lower troposphere due to its reduced signal-to-noise ratio. There may be a possible low-level

267   CTH solution (4C) having $P_c \geq 600$ hPa, which would require the window technique and/or a

268   more robust cloud retrieval algorithm, but that is beyond the scope of this study. Here in this

269   paper, we only focus on the results derived from the SCO2AT and MCO2AT. Note that from

270   Step 1D, a SCO2AT-retrieved P_c is considered valid only when it is smaller than a threshold

271   at 600 hPa or $P_g - 300$hPa (the smaller of the two). From Step 2D, the MCO2AT is invoked

272   only when the observed 13.3-μm radiance (R_{pix}^{Ch6}) is smaller than the modeled 13.3-μm

273   radiance (R_{ebg}^{Ch6}) by more than a threshold of $\delta_R^{Ch6} = 0.1$ Wm^{-2}sr^{-1}μm^{-1}. This also means that,

274   if $R_{pix}^{Ch6} > R_{ebg}^{Ch6} - \delta_R^{Ch6}$, the SCO2AT-retrieved P_c is adopted and no MCO2AT is invoked. The

275   threshold $\delta_R^{Ch6} = 0.1$ Wm^{-2}sr^{-1}μm^{-1} used here is slightly larger than five times the instrument

276   noise level of the GOES-12 imager 13.3-μm channel.

277   It is worth noting that the aforementioned iterative retrieval procedure is applicable to

278   all single-layer and multilayer cloud pixels, except that the MCO2AT works more effectively

279   for transmissive cirrus clouds in multilayer situations or geometrically thick, tenuous clouds.

280   Figure 1 schematically illustrates the main differences between SCO2AT (Figs. 1a-1c, left

281   side) and MCO2AT (Figs. 1d-1f, right side) and the various impacts of the effective

282 background radiances on three representative cases, namely 1) cirrus-overlying-stratus cloud

283 (Figs. 1a and 1d), 2) geometrically thick, optically thin cloud (Figs. 1b and 1e), and 3)

284 convective cloud (Figs. 1c and 1f). In the figure, all upper clouds are treated as a

285 geometrically thin layer with uniform $[P_c, T_c]$. The SCO2AT cases on the left side depict the

286 single-layer assumption with a fixed background level $[P_g, T_g]$ and the MCO2AT cases on

287 the right side show the modified assumption with an enhanced background level $[P_{ebg}, T_{ebg}]$.

288 For the cirrus-overlying-stratus cloud situation (Figs. 1a and 1d), the effective background

289 level is higher than the ground level (i.e., $P_{ebg} < P_g$) and the MCO2AT-inferred CTH (P_c in

290 Fig. 1d) is raised higher than the SCO2AT-inferred CTH (P_c in 1a). For the geometrically

291 thick, but optically thin cloud situation (Figs.1b and 1e), the effective background level is also

292 higher than the ground level and likewise the MCO2AT-inferred CTH (P_c in Fig. 1e) is also

293 higher than the SCO2AT-inferred CTH (P_c in Fig. 1b).

294   However, for the third situation of a convective cloud (Figs. 1c and 1f), despite the

295 effective background level being much higher than the ground level, the MCO2AT-inferred

296 CTH (P_c in Fig. 1f) is only slightly higher than the SCO2AT-inferred CTH (P_c in Fig. 1c).

297 This is because the convective cloud is more opaque than the upper transmissive clouds in the

298 previous two situations. Hence, the upper CTHs inferred by both MCO2AT and SCO2AT are

299 less sensitive to the different effective background radiances. We need to note that for opaque

300 upper clouds, the MCO2AT retrieval procedure as in Step 3D prevents the effective

301 background level from going too high in altitude. As such, a midway threshold chosen to be

302 between the clear-sky and overcast radiances, i.e., $R_{ebg}^{Ch4} = (R_{clr}^{Ch4} + R_{ovc}^{Ch4})/2$, is used to

303 constrain a minimum P_{ebg} for the upper bound and a threshold at the maximum $P_{ebg} = P_g$,

13

304   where $R_{ebg}^{Ch4} = R_{clr}^{Ch4}$ and surface emissivity = 1 are used to constrain the lower bound at the

305   surface level. As a result, for opaque upper clouds similar CTHs are inferred from both the

306   MCO2AT and SCO2AT.

307

308   **3. Data**

309   **3.1. Model Data**

310   The input atmospheric profiles of temperature, pressure, height, and moisture for

311   calculating the clear-sky, overcast, and effective background radiances (R_{clr}^{λ} , R_{ovc}^{λ} and R_{ebg}^{λ})

312   are taken from the NOAA National Centers for Environmental Prediction (NCEP) 1-hourly

313   Rapid Update Cycle (RUC) model-analysis dataset with a 40-km spatial resolution [Benjamin

314   et al., 2004a, b]. The hourly RUC data cover a large portion of North America including the

315   Contiguous United States (CONUS). The widely-used MODTRAN4 radiative transfer code

316   [Berk et al., 1999] is used for simulations of the spectral radiances. For the spectral cloud

317   emissivities at 10.7- and 13.3-μm channels, they are related through the adoption of an

318   average extinction coefficient ratio of $\sigma_{ext}^{Ch6}/\sigma_{ext}^{Ch4}$ = 1.12 (c.f. Eq. (13)) for an approximate

319   range of $\sigma_{ext}^{Ch6}/\sigma_{ext}^{Ch4}$ = 1.02-1.25 for various non-spherical ice crystal sizes [Yang et al., 2001].

320   This average extinction coefficient ratio results in an increase of approximately 10% in the

321   calculated cloud emissivity ratio $\varepsilon_{ext}^{Ch6}/\varepsilon_{ext}^{Ch4}$ (c.f. Eq. (12)).

322

323   **3.2. GOES-12 and ARSCL Data**

324   To evaluate the performance of the MCO2AT-retrieved CTHs via comparisons with

325   the ARSCL-derived CTHs, this study uses the half-hourly GOES-12 imagery data (scanning

14

326   at about 15 and 45 minutes of the UTC hour) obtained during the month of May 2005.

327   During this month, the ARM field research location at the Southern Great Plains (SGP) Cloud

328   and Radiation Test Bed (CART) site in Lamont, Oklahoma was frequently cloudy, having

329   various cloud types almost every day. The half-hourly GOES-12 imagery data for the SGP

330   domain were taken from the NASA Langley ARM imagery and cloud product archives

331   [Ayers et al., 2006; see http://www-angler.larc.nasa.gov/]. Those images have a convolved 4

332   km × 3.2 km spatial resolution at nadir. The original scanning resolution is about 4 km × 2.3

333   km (north-south direction × east-west direction) for the 10.7-μm channel and about 8 km ×

334   2.3 km (north-south × east-west) for the 13.3-μm channel. At the ARM SGP CART site

335   [36.6°N, 97.5°W], the GOES-12 imager has an oblique satellite viewing zenith angle of ~48°

336   and this degrades its spatial resolution by approximately a factor of 1.5 compared to the nadir.

337   The ARSCL data products provide a time series of ground-based observations of

338   cloud-top and cloud-base heights for single-layer or multilayer clouds observed at the ARM

339   SGP CART site [Clothiaux et al., 2000]. The ARSCL algorithm combines the ground-based

340   active remote sensing measurements from both a millimeter-wavelength cloud radar (MMCR)

341   and a micro-pulse lidar (MPL) to estimate the locations of cloud-top and cloud-base heights at

342   an up-looking spatial resolution of ~45 m and a temporal sampling rate at 10-second intervals.

343   The ARSCL produces a much finer-resolution time series data than the half-hourly GOES-12

344   imager data. But at each observation time, the GOES-12 imager views a much larger cloud

345   area than that viewed by the vertically pointing narrow-beamed ARSCL radar and lidar.

346   Meticulous comparisons between the satellite- and ground-based cloud observations are

347   needed to minimize the uncertainties in matching the data obtained from two different

348   platforms.

349

4. Comparisons

4.1. Comparisons of MCO2AT and SCO2AT CTPs

350

351

352   Figures 2 and 3 are used to demonstrate the SCO2AT and MCO2AT inferred CTPs.

353   Figure 2 shows an example of the GOES-12 imagery data for the 13.3-μm (2a) and 10.7-μm

354   (2b) channels obtained at 10:45 UTC on 1 May 2005 for SGP spatial domain, which extends

355   from 32°N to 42°N and from 105°W to 91°W. The ARM SGP CART site is indicated by the

356   little square near the center of the images. In Fig. 2a, the 13.3-μm brightness temperatures are

357   obscured by the CO_2 absorption and thus appear colder (brighter) than the 10.7-μm brightness

358   temperatures in Fig. 2b. Figure 3 shows the corresponding SCO2AT-inferred P_c (Fig. 3a)

359   and P_g (Fig. 3b) and MCO2AT-inferred P_c (Fig. 3c) and P_{ebg} (Fig. 3d) for the images shown

360   in Fig. 2. The MCO2AT-inferred P_c (Fig. 3c) are generally smaller (higher in altitude) than

361   the SCO2AT-inferred P_c in Fig. 3a. Similarly, the MCO2AT-inferred P_{ebg} values in Fig. 3d

362   are generally less than P_g in Fig. 3b.

363   In this example (Figs. 2 and 3), the upper clouds do not appear to be opaque as

364   evidenced by the relatively low MMCR reflectivities seen between 5 and 11 km in Figure 4,

365   which shows the corresponding MMCR reflectivity profiles obtained at the SGP CART site

366   on this day. Note that the MMCR reflectivity profiles are plotted in reverse UTC time so that

367   the reflectivity profiles for the time prior to 10:45 UTC (GOES-12 image time) are plotted

368   eastwards to correspond with the GOES-12 image clouds on the east side of the SGP CART

369   site, and likewise the reflectivity profiles for the time after 10:45 UTC are plotted westwards

370   to correspond with the GOES-12 image clouds on the west side of the SGP CART site.

16

371   Figure 4 shows that the clouds extend vertically several kilometers and the upper clouds are

372   sometimes contiguous with but sometimes decoupled from the lower clouds. Such vertical

373   extensions and split cloud layers make the satellite cloud retrieval difficult when the single-

374   layer and/or the geometrically thin layer assumptions are used. Both assumptions result in

375   underestimations of satellite-inferred CTH; for example, the larger SCO2AT-inferred P_c by

376   assuming a clear background level at P_g than the relatively smaller MCO2AT-inferred P_c .

377   Figure 5 compares the differences between the MCO2AT- and SCO2AT-inferred P_c

378   (5a) and the differences between their corresponding P_{ebg} and P_g (5b) for the cloud pixels

379   shown in Fig. 3. In the figure, when both MCO2AT and SCO2AT have the same P_c , the

380   retrieval Steps 2A-2D were used and their associated values of P_{ebg} and P_g are also identical.

381   For pixels having P_c from MCO2AT that are smaller than their SCO2AT counterparts,

382   retrieval Steps 3A-3H were invoked and the associated mean (standard deviation) P_c is about

383   381 (79) hPa for the MCO2AT and 451 (91) hPa for the SCO2AT. Their corresponding P_{ebg}

384   and P_g means (standard deviation) are about 703 (61) hPa and 944 (43) hPa, respectively.

385   The MCO2AT significantly decreased the upper-cloud P_c and the mean difference (standard

386   deviation) of MCO2AT minus SCO2AT is about -70 (37) hPa for P_c and -241 (65) hPa for

387   P_{ebg} minus P_g .

388   Figure 6 shows GOES-12 13.3-μm (Fig. 6a) and 10.7-μm (Fig. 6b) images obtained at

389   10:45 UTC, 24 May 2005, when a deep convective storm system occupied a sizeable portion

390   of the scene. Again, the associated SCO2AT-inferred P_c (Fig. 7a) and P_g (Fig. 7b) values

391   exceed their MCO2AT-inferred P_c (Fig. 7c) and P_{ebg} (Fig. 7d) counterparts. Figure 8 shows

392 the corresponding SGP CART MMCR reflectivity profiles. Although such convective

393 systems are generally thought to have more opaque cloud tops, the upper clouds as revealed in

394 Fig. 8 have generally low radar reflectivities (negatives in dBZ) that do not appear as opaque

395 as expected. The low or missing radar reflectivities are likely caused by attenuation by the

396 lower clouds and by the inability of cloud radars to detect the small ice crystals and low ice

397 water contents in the top portions of those clouds [e.g., McGill et al., 2004].

398   For the cloudy pixels in Figure 7, the mean difference (standard deviation) between

399 the values of P_c from MCO2ATand SCO2AT is about -60 (40) hPa and the corresponding

400 mean difference (standard deviation) of P_{ebg} minus P_g is about -318 (113) hPa. The

401 differences between the MCO2AT- and SCO2AT-inferred P_c are substantial even around the

402 central areas of the deep convective clouds (c.f. Figs. 7a and 7c).

403

404 **4.2. Comparisons with ARSCL CTHs**

405   In order to compare with the ARSCL CTH data, the MCO2AT- and SCO2AT-

406 retrieved pixel-scale P_c are first converted to CTH z_c using the RUC vertical profiles of

407 atmospheric pressure. Secondly, from each half-hourly GOES image analysis, spatial

408 averages of z_c from the MCO2AT- and SCO2AT were computed based on the imager pixels

409 obtained within a 15 km $\times$15 km area centered at the SGP CART site. Figure 9 shows the

410 half-hourly mean z_c values from the MCO2AT (solid points) and SCO2AT (cross points)

411 obtained on 1 May (9a) and 24 May (9b) 2005, along with the ARSCL time-series cloud

412 vertical profile mask plotted in grey areas. Both Figs. 9a and 9b are also plotted in reverse

18

413 UTC time, in the same manner used for the MMCR reflectivity profiles in Fig. 4 and Fig. 8, to

414 reflect the east-west cloud orientation in satellite images.

415   The differences between the MCO2AT- and SCO2AT-inferred mean z_c is

416 approximately 2 km at 10:45 UTC on May 1 (Fig. 9a) and is slightly less than 1 km at 10:45

417 UTC on May 24 (Fig. 9b). In the figure, the solid circles indicate that 100% of the pixels

418 within the 15-km area had valid MCO2AT and SCO2AT retrievals whereas the solid triangles

419 indicate that only a portion of the pixels in the 15-km area had valid MCO2AT and SCO2AT

420 retrievals. (More details on the overcast and broken cloud scenes are presented later in Fig.

421 10.) The MCO2AT-inferred mean z_c values show generally good agreement with the

422 ARSCL uppermost CTHs, whereas the SCO2AT-inferred mean z_c values are generally lower

423 than the MCO2AT mean z_c by about 1-2 km. Some of the differences between the

424 MCO2AT and SCO2AT mean z_c and the ARSCL data in Fig. 9b are larger than 3 km near

425 the cloud edges or when the upper clouds are thin.

426   To evaluate the performance of the MCO2AT relative to the SCO2AT, we analyzed a

427 total of 1488 half-hourly data from the GOES-12 imager obtained during 1-31 May 2005 and

428 examined both the MCO2AT and SCO2AT retrievals for the 15-km area at the SGP site. To

429 facilitate the comparisons, the 1488 half-hourly 15-km scenes were divided into different

430 categories according to both the imager-retrieved pixel z_c and the ARSCL uppermost CTH

431 data within ±1.5 minutes of the GOES-12 imager scan time at the SGP CART site

432 (approximately at 17 and 47 minutes after the UTC hour). The first category, the overcast

433 upper-cloud scene (solid circles in Fig. 9), requires that 100% of the GOES-12 imager pixels

434 within the 15-km area have valid z_c retrievals from both MCO2AT and SCO2AT and 100%

435   of the ARSCL profile data within the ±1.5-min period of the imager scan-passing time must

436   have a valid uppermost CTH greater than 4.3 km (~600 hPa) at every shot. The second

437   category, the broken upper-cloud scene (solid triangles in Fig. 9), requires that either the

438   GOES-12 imager pixels only have a portion with valid z_c retrievals in the 15-km area or the

439   ARSCL profiles only have a portion with valid uppermost CTH greater than 4.3 km within

440   the ±1.5-min period. The third category is called the border upper-cloud scene (as marked by

441   open triangles in Fig. 11). In this category, the GOES-12 imager pixels have some valid z_c

442   and the ARSCL profiles have no CTH > 4.3 km within the ±1.5-min period, but have some

443   valid CTH > 4.3 km in a bigger window of ±3-min period.

444   Among the 1488 cases, we found 377 cases that were overcast upper-cloud scenes,

445   248 cases had broken upper-cloud scenes, 26 cases had border upper-cloud scenes, and 16

446   cases had missing data. There were also 196 cases having ARSCL profiles with valid CTH >

447   4.3 km within the ±1.5-min period but with no valid MCO2AT and SCO2AT z_c in the 15-km

448   area. These cases are generally optically thin clouds with MMCR reflectivities less than −20

449   dBZ and, in many of the cases, it was necessary to widen the area to find valid z_c retrievals in

450   the neighborhood. Those cases are not included in this study.

451   Figure 10 shows the one-to-one comparisons between the ARSCL and the MCO2AT

452   (left column) and SCO2AT (right column) obtained mean CTHs for 1) overcast upper-cloud

453   scenes (a and b), 2) broken upper-cloud scenes (c and d), and 3) border upper-cloud scenes (e

454   and f). Here the mean ARSCL upper CTHs are obtained by averaging the 25th–75th

455   percentiles of all valid uppermost CTHs > 4.3 km in the ±1.5-min period. The vertical bars in

456   the figure indicate the range of the 25th–75th percentiles. The mean MCO2AT and SCO2AT

457   CTHs are obtained by averaging all valid pixel-retrieved z_c within ±3 standard deviations of

458   the mean value. For reference, the solid circles in Figs. 10a and 10b denote the overcast

459   upper-cloud scenes obtained on both 1 May (Fig. 9a) and 24 May (Fig. 9b) and the solid

460   triangles in Figs. 10c and 10d denote the broken upper-cloud scenes also obtained on the two

461   days.

462   The results obtained here show significant improvements in CTH from the MCO2AT

463   compared to the SCO2AT for overcast and broken upper-cloud scenes. Mean biases of the

464   MCO2AT minus ARSCL CTHs are −0.33 km ± 1.54 km for the overcast (Fig. 10a) and −2.66

465   km ± 1.80 km for the broken scenes (10c). For SCO2AT minus ARSCL, the mean biases in

466   CTH are −1.58 km ± 2.08 km for the overcast (10b) and −4.73 km ± 2.28 km for the broken

467   scenes (10d). From Figs. 10a and 10b, it is worth mentioning that many MCO2AT- and

468   SCO2AT-inferred CTHs are significantly larger than the ARSCL uppermost CTHs. We

469   examined the MMCR reflectivities for these cases and found that they are mostly from

470   precipitating convective clouds as revealed by relatively large dBZ values. Many of these

471   cases are found on May 13, 23, 26, and 31 and the ARSCL uppermost CTHs were

472   considerably lower than the MCO2AT- and SCO2AT-inferred mean CTHs.

473   Figure 11 shows the results for May 26. Between about 10:00 and 12:00 UTC, the

474   ARSCL uppermost CTHs are systematically several kilometers lower than the MCO2AT and

475   SCO2AT overcast upper CTHs. Most likely, the differences are due to attenuation of the

476   cloud radar and lidar beams and the limitations of the radar for detecting small particles, as

477   discussed earlier. In addition, Fig. 11 also shows two border upper-cloud scenes denoted by

478   the open triangles at 05:47 and 15:47 UTC, which are among the 26 cases shown in Figs. 10e

479   and 10f. For these border upper-cloud scenes, the mean ARSCL upper CTHs obtained in the

480   ±1.5-min period are lower than 4.3 km and much lower than the MCO2AT and SCO2AT

481   inferred CTHs.

482   Lastly, Figure 12 shows the histograms of the CTH differences for the comparisons

483   obtained in Figs. 10a-10d. For the overcast upper-cloud scenes (Fig. 12a), the SCO2AT

484   minus ARSCL difference is within ±0.5 km in 21% of the cases and within ±1.5 km for 48%

485   of the comparisons. For the MCO2AT cases, the differences within ±0.5 and ±1.5 km are

486   improved to 31% and 69%, respectively. Figure 12b shows the comparisons for broken

487   upper-cloud scenes. In the SCO2AT minus ARSCL cases, about 20% are within ±3 km,

488   which is improved to more than 50% for the MCO2AT cases.

489   It is clear from these results that the MCO2AT retrieves a value of CTH that is closer

490   to the physical top of the cloud than that obtained with most other passive retrieval methods.

491   Traditionally, the retrieved value of CTH has been associated with the altitude corresponding

492   to the effective radiating temperature of the cloud. For optically thick clouds, that value

493   corresponds more closely to the height at approximately 1 optical depth below the physical

494   cloud top. For optically thin clouds, the retrieved depth is associated with the height of a

495   smaller optical depth. Although some empirical methods have been developed to account for

496   this difference using the window techniques [Minnis et al., 2008, 2009], more evaluation is

497   needed to employ them reliably. By directly retrieving the physical height of the cloud top,

498   the MCO2AT may obviate the need for such corrections.

499

500   **5. Concluding Remarks**

501   The difficulties of inferring upper cloud top heights (CTHs) for optically thin clouds

502   using passive meteorological satellite data are well known. For upper transmissive clouds, the

22

503   inferences become more difficult in multilayer cloud situations when lower clouds coexist

504   underneath the upper clouds. Operational meteorological satellite analyses have shown much

505   success in using the CO_2-slicing or CO_2-absorption techniques to retrieve the CTH

506   information for transmissive cirrus clouds, but all current retrieval algorithms are based on

507   single-layer cloud assumptions. That is, they commonly assume that the cloud layer occupies

508   an infinitesimal thickness in vertical extent and that underneath the geometrically thin cloud

509   layer is a cloud-free atmosphere over the surface.

510   The single-layer assumptions may induce large uncertainties in the satellite-inferred

511   CTHs because cloud vertical profiles, as revealed by the data obtained from the cloud radar

512   and lidar, are often complex and a single-layer cloud with a geometrically thin thickness is

513   relatively infrequent. To overcome the difficulties with conventional single-layer

514   assumptions, a new method for inferring the upper CTH using a modified CO_2-absorption

515   technique (MCO2AT) has been presented in this paper. This new method employs a three-

516   step sequential retrieval procedure that starts with the single-layer CO_2-absorption technique

517   (SCO2AT) followed by iterative retrieval processes to obtain an enhanced upper CTH. The

518   modified method described in this paper was applied to GOES-12 imager 10.7- and 13.3-µm

519   data and is applicable to data from instruments on other satellites having similar spectral

520   bands. These would include the Spinning Enhanced Visible and Infrared Imager (SEVIRI)

521   onboard Meteosat-8 and -9 and the Moderate-resolution Imaging Spectroradiometer (MODIS)

522   on *Terra* and *Aqua*.

523   Comparisons between the MCO2AT- and SCO2AT-inferred CTHs and the ARM

524   ground-based ARSCL data demonstrated that the MCO2AT was more effective when the

525   upper portion of a cloud is optically thin but geometrically thick and when an upper cirrus

526 cloud overlaps with some lower stratus or cumulus clouds. The MCO2AT CTH retrievals

527 represent a significant improvement over the SCO2AT CTH values. Based on comparisons

528 using one month of half-hourly GOES-12 retrievals and the ARSCL data, the mean biases in

529 the GOES-12-inferred upper CTHs were reduced from -1.6 km (SCO2AT) to -0.3 km

530 (MCO2AT) for overcast upper-cloud scenes and from -4.7 km (SCO2AT) to -2.7 km

531 (MCO2AT) for broken upper-cloud scenes. Since the MCO2AT retrieved more accurate

532 upper CTHs, the overall distributions of the upper cloud amounts were enhanced at higher

533 altitudes and the associated root-mean-square errors were also reduced by 30% relative to the

534 SCO2AT retrievals. However, more than 10% of the thin cirrus cloud cases detected by

535 ARSCL were not retrieved by MCO2AT and SCO2AT. This suggests that a more sensitive

536 method is needed to retrieve these thin cirrus clouds. Nevertheless, the comparisons obtained

537 here have provided a preliminary validation for the MCO2AT-inferred CTHs and have shown

538 better agreement with ground-based radar and lidar data, especially for multilayer clouds and

539 optically thin but geometrically thick clouds. Future research plans include applications to

540 other satellite data and additional comparisons with surface and space-based active remote

541 sensing measurements to determine the accuracy of the method over a wide range of cloud,

542 surface, and weather conditions.

543

544

549 **References**

550 Ackerman, T. P., and G. Stokes (2003), The Atmospheric Radiation Measurement Program,

551   *Physics Today*, *56*, 38-45.

552 Ayers, J. K., et al. (2006), Overview of NASA Langley ARM cloud products and validation,

553   *Proc. 16th ARM Sci. Team Mtg.*, Albuquerque, NM, March 27-31.

554   (http://www.arm.gov/publications/proceedings/conf16/extended_abs/ayers_jk.pdf)

555 Bedka, S. T., W. F. Feltz, A. J. Schreiner, and R. E. Holz (2007), Satellite-derived cloud top

556   pressure product validation using aircraft-based cloud physics lidar data from the

557   ATReC field campaign, *Int. J. Rem. Sens.*, *28*, 2221-2239.

558 Benjamin, S. G., G. A. Grell, J. M. Brown, T. G. Smirnova, and R. Bleck (2004a), Mesoscale

559   weather prediction with the RUC hybrid isentropic–terrain-following coordinate model,

560   *Mon. Weather Rev.*, *132*, 473-494.

561 Benjamin, S. G., et al. (2004b), An hourly assimilation–forecast cycle: The RUC, *Mon.*

562   *Weather Rev.*, *132*, 495-518.

563 Berk, A., et al. (1999), MODTRAN4 v. 2.0 User's Manual, Air Force Geophysics Laboratory

564   Tech. Rep. AFGL-TR-89-0122. 98 pp., Air Force Mat. Comm., Hanscomb AFB, Mass..

565 Chang, F.-L., and Z. Li (2005), A near-global climatology of single-layer and overlapped

566   clouds and their optical properties retrieved from Terra/MODIS data using a new

567   algorithm, *J. Climate*, *18*, 4752-4771.

568 Chahine, M. T. (1974), Remote sounding of cloudy atmospheres. I. The single cloud layer, *J.*

569   *Atmos. Sci.*, *31*, 233-243.

570 Clothiaux, E. E., T. P. Ackerman, G. G. Mace, K. P. Moran, R. T. Marchand, M. Miller, and

571   B. E. Martner (2000), Objective determination of cloud heights and radar reflectivities

572   using a combination of active remote sensors at the ARM CART Sites, *J. Appl.*

573   *Meteorol.*, *39*, 645-665.

574 Eyre, J. R., and W. P. Menzel (1989), Retrieval of cloud parameters from satellite sounder

575   data: A simulation study, *J. Appl. Meteorol.*, *28*, 267-275.

576 Frey, R. A., B. A. Baum, W. P. Menzel, S. A. Ackerman, C. C. Moeller, and J. D. Spinhirne

577   (1999), Validation of CO_2-slicing cloud heights computed from MAS radiance data

578   during SUCCESS, *J. Geophys. Res.*, *104*, 24,547-24,555.

579 Hawkinson, J. A., W. F. Feltz, and S. A. Ackerman (2005), A comparison of GOES sounder

580   and cloud lidar- and radar-retrieved cloud-top heights, *J. Appl. Meteorol.*, *44*, 1234-1242.

581 Holz, R. E., S. Ackerman, P. Antonelli, F. Nagle, R. O. Knuteson, M. McGill, D. L. Hlavka,

582   and W. D. Hart (2006), An improvement to the high-spectral-resolution CO_2-slicing

583   cloud-top altitude retrieval, *J. Atmos. Oceanic Technol.*, *23*, 653-670.

584 Jin, Y., W. B. Rossow, and D. P. Wylie (1996), Comparison of the climatologies of high-level

585   clouds from HIRS and ISCCP, *J. Climate*, *9*, 2850-2879.

586 McCleese, D. J., and L. S. Wilson (1976), Cloud top heights from temperature sounding

587   instruments, *Q. J. R. Meteorol. Soc.*, *102*, 781-790.

588 McGill, M. J., L. Li, W. D. Hart, G. M. Heymsfield, D. L. Hlavka, P. E. Racette, L. Tian, M.

589   A. Vaughan, D. M. Winker (2004), Combined lidar-radar remote sensing: Initial results

590   from CRYSTAL-FACE, *J. Geophys. Res.*, *109*, D07203, doi:10.1029/2003JD004030.

591 Menzel, W. P., W. L. Smith, and T. R. Stewart (1983), Improved cloud motion vector and

592   altitude assignment using VAS, *J. Climate Appl. Meteorol.*, *22*, 377-384.

593   Menzel, W. P., D. P. Wylie, and K. I. Strabala (1992), Seasonal and diurnal changes in cirrus

594   clouds as seen in four years of observations with the VAS, *J. Appl. Meteorol.*, *31*, 370-

595   385.

596   Menzel, W. P., and J. F. W. Purdom (1994), Introducing GOES-I: The first of a new

597   generation of geostationary operational environmental satellites, *Bull. Am. Meteorol.*

598   *Soc.*, *75*, 757-781.

599   Minnis, P., K.-N. Liou, and Y. Takano (1993), Inference of cirrus cloud properties using

600   satellite-observed visible and infrared radiances. Part I: Parameterization of radiance

601   field, *J. Atmos. Sci.*, *50*, 1279-1304.

602   Minnis, P., D. P. Garber, D. F. Young, R. F. Arduini, and Y. Takano (1998), Parameterization

603   of reflectance and effective emittance for satellite remote sensing of cloud properties, *J.*

604   *Atmos. Sci.*, *55*, 3313-3339.

605   Minnis, P., et al. (2009), Cloud property retrievals for CERES using TRMM VIRS and Terra

606   and Aqua MODIS data, *IEEE Trans. Geosci. Remote Sens.*, submitted.

607   Minnis, P., C. R. Yost, S. Sun-Mack, and Y. Chen (2008), Estimating the physical top altitude

608   of optically thick ice clouds from thermal infrared satellite observations using CALIPSO

609   data, *Geophys. Res. Lett.*, *35*, L12801, doi:10.1029/2008GL033947.

610   Rossow, W. B. (1989), Measuring cloud properties from space: A review, *J. Climate*, *2*, 201-

611   213.

612   Rossow, W. B., and R. A. Schiffer (1991), ISCCP cloud data products, *Bull. Am. Meteorol.*

613   *Soc.*, 72, 2-20.

614   Rossow, W. B., and R. A. Schiffer (1999), Advances in understanding clouds from ISCCP,

615   *Bull. Am. Meteorol. Soc.*, *80*, 2261-2287.

616 Schmit, T. J., E. M. Prins, A. J. Schreiner, and J. J. Gurka (2001), Introducing the GOES-M

617   imager, *National Weather Assoc. Digest*, *25*, 28-37.

618 Schreiner, A., T. Schmit, and W. Menzel (2001), Observations and trends of clouds based on

619   GOES sounder data, *J. Geophys. Res.*, *106*, 20,349-20,363.

620 Smith, W. L., and R. A. Frey (1990), On cloud altitude determinations from high resolution

621   interferometer sounder (HIS) observations, *J. Appl. Meteorol.*, *29*, 658-662.

622 Smith, W. L., and C. M. R. Platt (1978), Comparison of satellite-deduced cloud heights with

623   indications from radiosonde and ground-based laser measurements, *J. Appl. Meteorol.*,

624   *17*, 1796-1802.

625 Smith, W. L., P. Minnis, H. Finney, R. Palikonda, and M. M. Khaiyer (2008), An evaluation

626   of operational GOES-derived single-layer cloud top heights with ARSCL over the ARM

627   Southern Great Plains site, *Geophys. Res. Lett.*, *35*, L13820, doi:10.1029/2008GL03427

628 Wielicki, B. A., and J. A. Coakley Jr. (1981), Cloud retrieval using infrared sounder data:

629   Error analysis. *J. Appl. Meteorol.*, *20*, 157-169.

630 Wylie, D. P., and W. P. Menzel (1989), Two years of cloud cover statistics using VAS, *J.*

631   *Climate*, *2*, 380-392.

632 Wylie, D. P., and W. P. Menzel (1999), Eight years of high cloud statistics using HIRS, *J.*

633   *Climate*, *12*, 170-184.

634 Yang, P., B.-C. Gao, B. A. Baum, Y. X. Hu, W. J. Wiscombe, S.-C. Tsay, D. M. Winker, and

635   S. L. Nasiri (2001), Radiative properties of cirrus clouds in the infrared (8-13 μm)

636   spectral region, *J. Quant. Spectro. Radiat. Trans.*, *70*, 473-504.
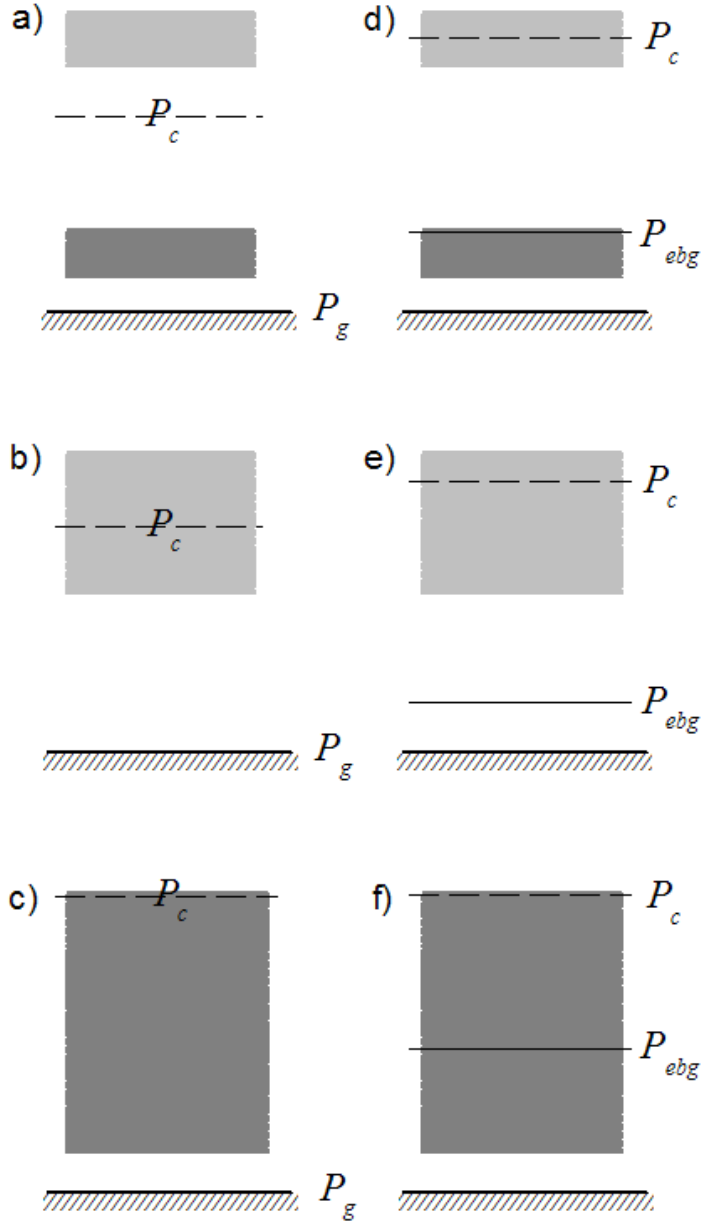
637

638

639 Fig. 1 Schematic diagrams of cirrus-overlying-stratus cloud (a, d), geometrically thick and

640   optically thin cloud (b, e), and convective cloud (c, f). P_c from SCO2AT shown on the

641   left (a-c) and P_c and P_{ebg} from MCO2AT are shown on the right (d-f). P_g is ground
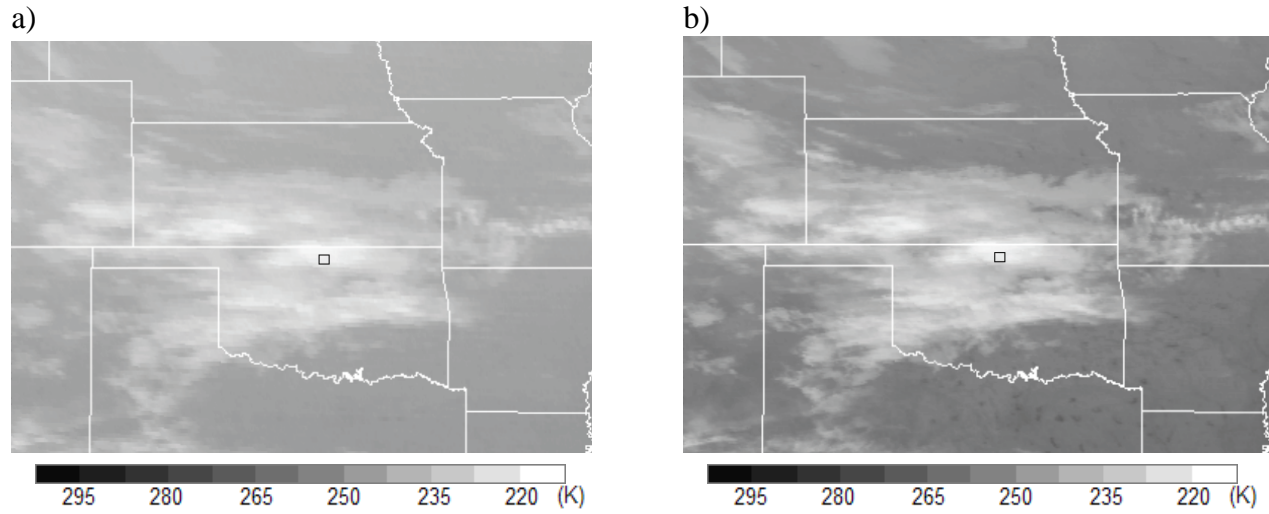
642   level.

643 Fig. 2 GOES-12 imager-observed a) 13.3-μm and b) 10.7-μm brightness temperatures, 1 May

644   2005, 10:45 UTC for an area of 32°N-42°N and 105°W-91°W. Square near the center

645   of the images marks the ARM SGP CART site.

646 Fig. 3 a) SCO2AT-inferred P_c, b) ground-level P_g, c) MCO2AT-inferred P_c, and d)

647   MCO2AT-inferred P_{ebg}. Results are obtained for the GOES-12 imager data shown in

648   Fig. 2.

649 Fig. 4 Vertical profiles of MMCR reflectivity (dBZ) obtained at the SGP CART site on 1

650   May 2005. Red arrow indicates scan time of the GOES-12 imager data in Figs. 2 and 3.

651 Fig. 5 Comparisons of a) MCO2AT-inferred P_c and SCO2AT-inferred P_c and b) MCO2AT-

652   inferred P_{ebg} and P_g.

653 Fig. 6 GOES-12 imager-observed a) 13.3-μm and b) 10.7-μm brightness temperatures

654   obtained on 24 May 2005 10:45 UTC for an area of 32°N-42°N and 105°W-91°W.

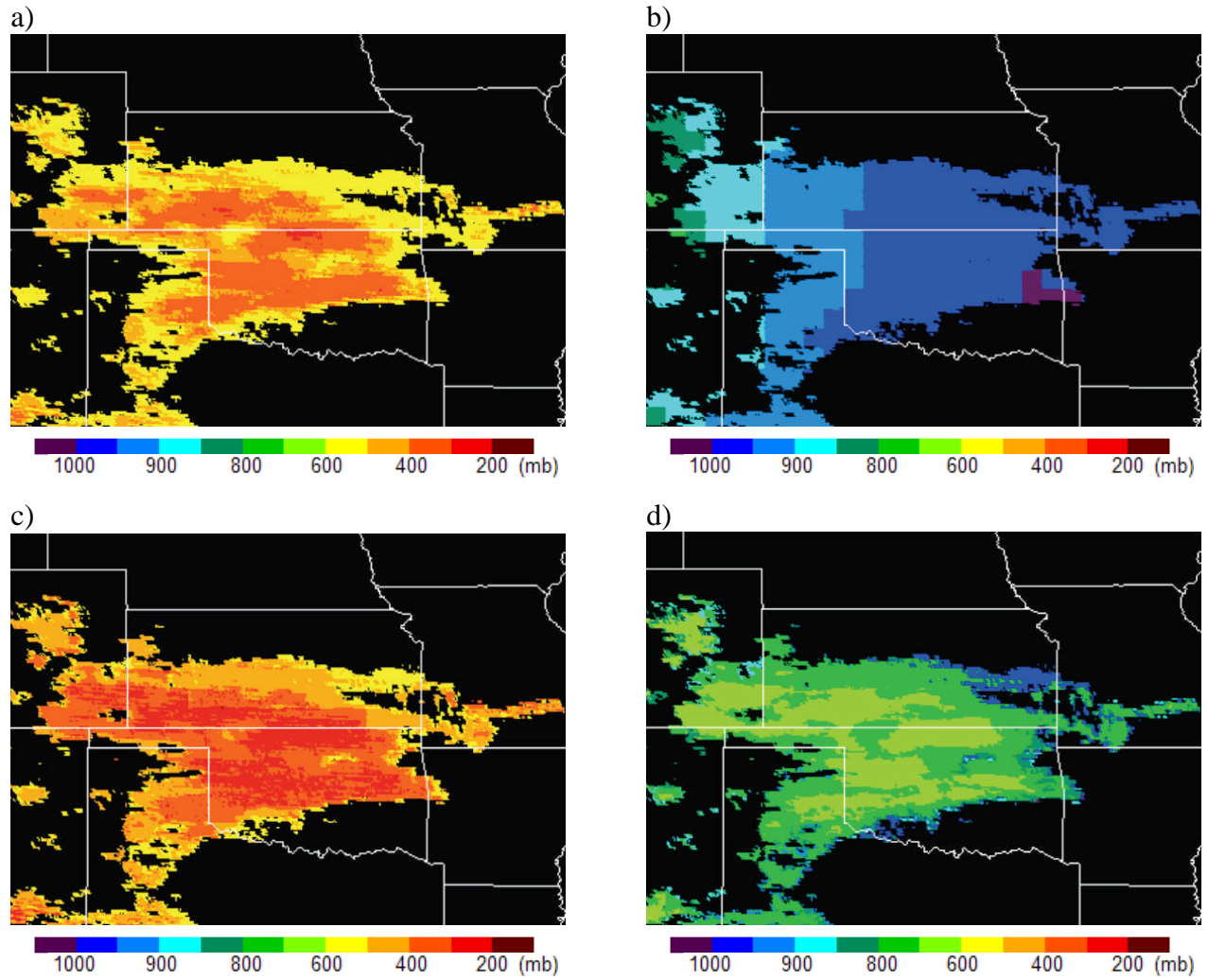655   Square near the center of the images marks the ARM SGP CART site.

656 Fig. 7 a) SCO2AT-inferred P_c, b) ground-level P_g, c) MCO2AT-inferred P_c, and d)

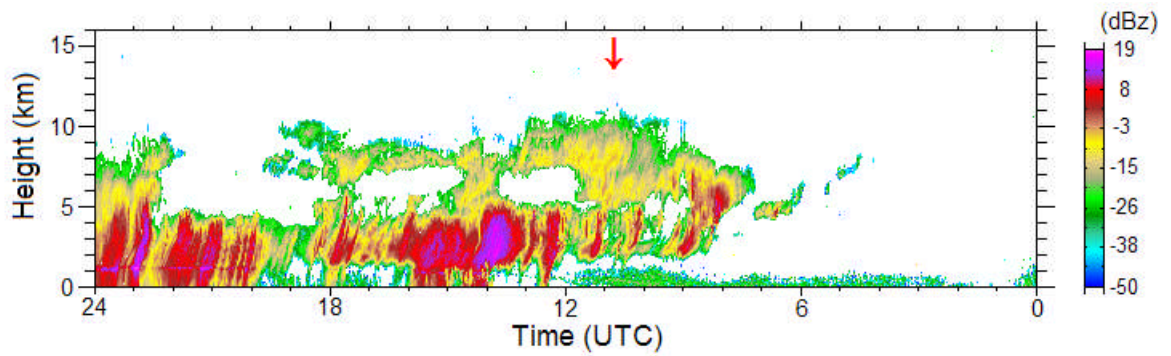657   MCO2AT-inferred P_{ebg}. Results are obtained for the GOES-12 imager data shown in

658   Fig. 6.

659　　　Fig. 8　Vertical profiles of MMCR reflectivity (dBZ) at ARM SGP CART site, 24 May 2005.

660　　　　　　Red arrow indicates scan time of the GOES-12 imager data in Figs. 6 and 7.

661　　　Fig. 9　MCO2AT-inferred CTHs (solid points) and SCO2AT-inferred CTHs (cross points)

662　　　　　　obtained on a) 1 May and b) 24 May 2005. Solid circles indicate overcast upper-cloud

663　　　　　　scenes and solid triangles indicate broken upper-cloud scenes. Grey areas are cloud

664　　　　　　masks constructed using the ARSCL data. Arrows indicate the time as shown in Figs.

665　　　　　　4 and 8.

666　　　Fig. 10　Comparisons of ARSCL upper CTHs and the MCO2AT (a, c, e) and SCO2AT (b, d, f)

667　　　　　　inferred CTHs for overcast upper clouds (a, b), broken upper clouds (c, d), and border

668　　　　　　upper clouds (e, f). Vertical bar indicates the 25th-75th percentiles of the ARSCL data.

669　　　Fig. 11　CTH retrieved using MCO2AT (solid and open circles) and SCO2AT (crosses) for 26

670　　　　　　May 2005. Solid circles indicate overcast upper-cloud scenes, solid triangles indicate

671　　　　　　broken upper-cloud scenes, and open triangles indicate border upper-cloud scenes.

672　　　　　　Grey areas are cloud masks constructed using the ARSCL data.

673　　　Fig. 12　Histograms of the upper CTH differences between MCO2AT minus ARSCL (filled

674　　　　　　grey) and SCO2AT minus ARSCL (no fill). a) for overcast upper-cloud scenes and b)

675　　　　　　for broken upper-cloud scenes.

676

Fig. 1 Schematic diagrams of cirrus-overlying-stratus cloud (a, d), geometrically thick and optically thin cloud (b, e), and convective cloud (c, f). P_c from SCO2AT shown on the left (a-c) and P_c and P_{ebg} from MCO2AT are shown on the right (d-f). P_g is ground level.
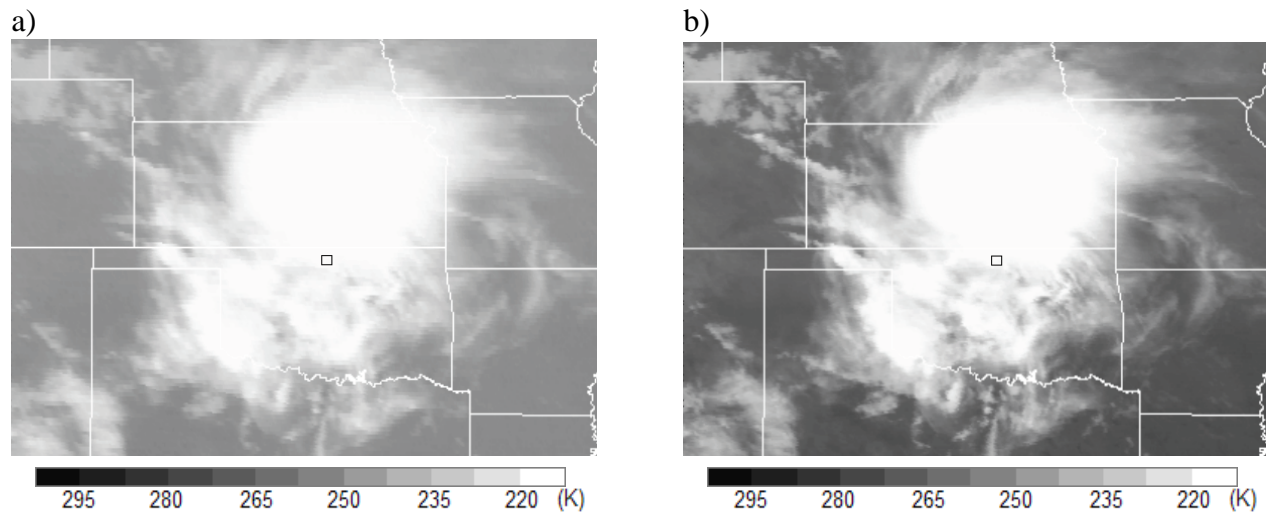
Fig. 2 GOES-12 imager-observed a) 13.3-μm and b) 10.7-μm brightness temperatures, 1 May 2005, 10:45 UTC for an area of 32°N-42°N and 105°W-91°W. Square near the center of the images marks the ARM SGP CART site
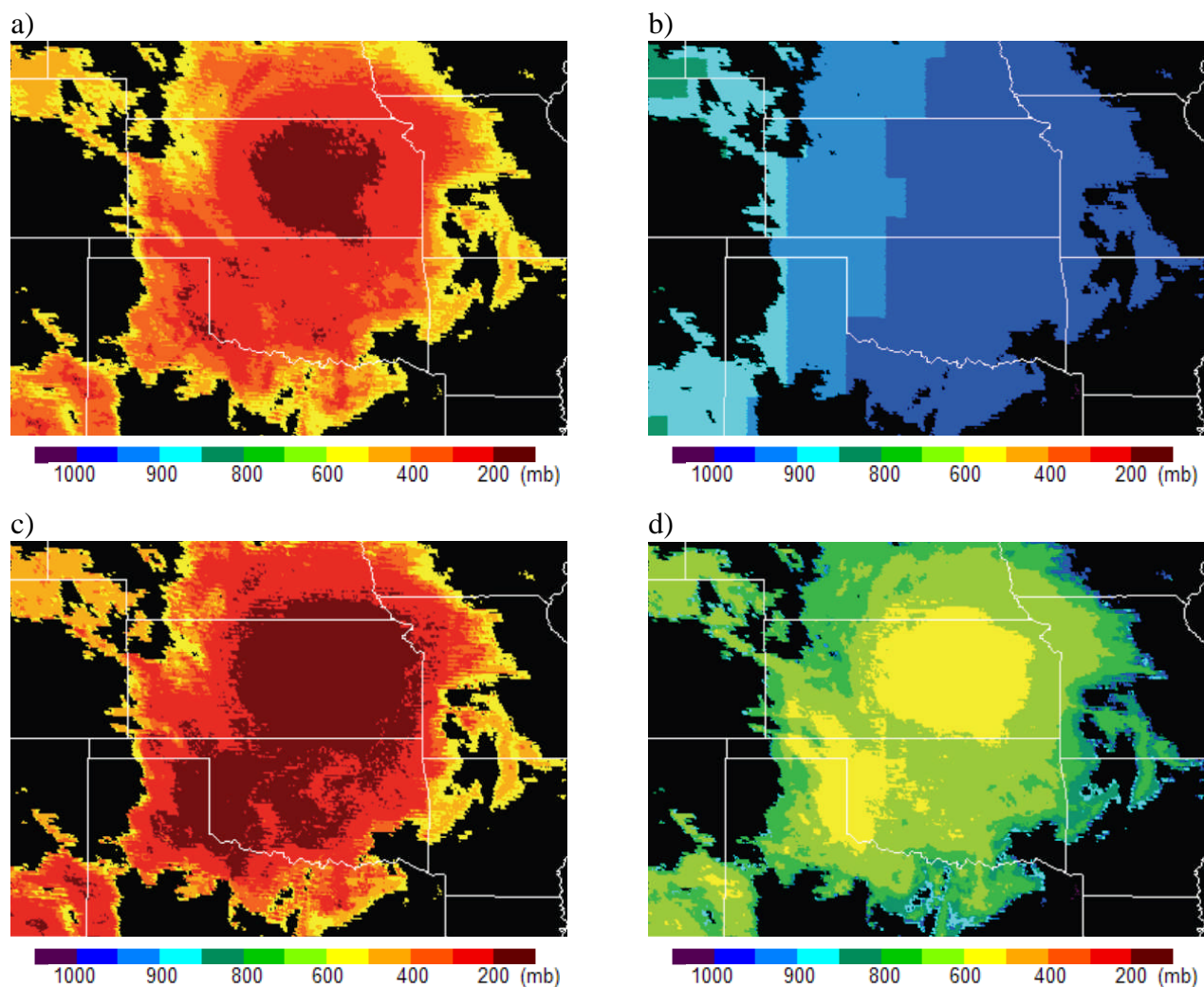
Fig. 3 a) SCO2AT-inferred P_c, b) ground-level P_g, c) MCO2AT-inferred P_c, and d) MCO2AT-inferred P_{ebg}. Results are obtained for the GOES-12 imager data shown in Fig. 2.
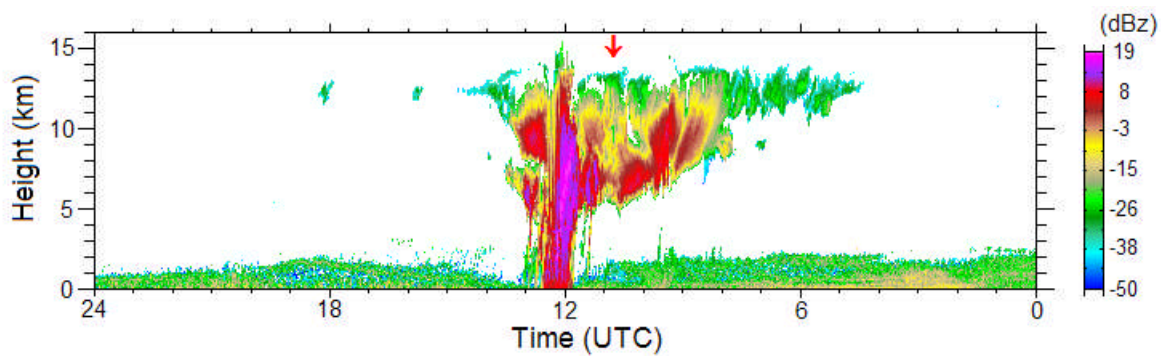

Fig. 4 Vertical profiles of MMCR reflectivity (dBZ) obtained at the SGP CART site on 1 May 2005. Red arrow indicates scan time of the GOES-12 imager data in Figs. 2 and 3.
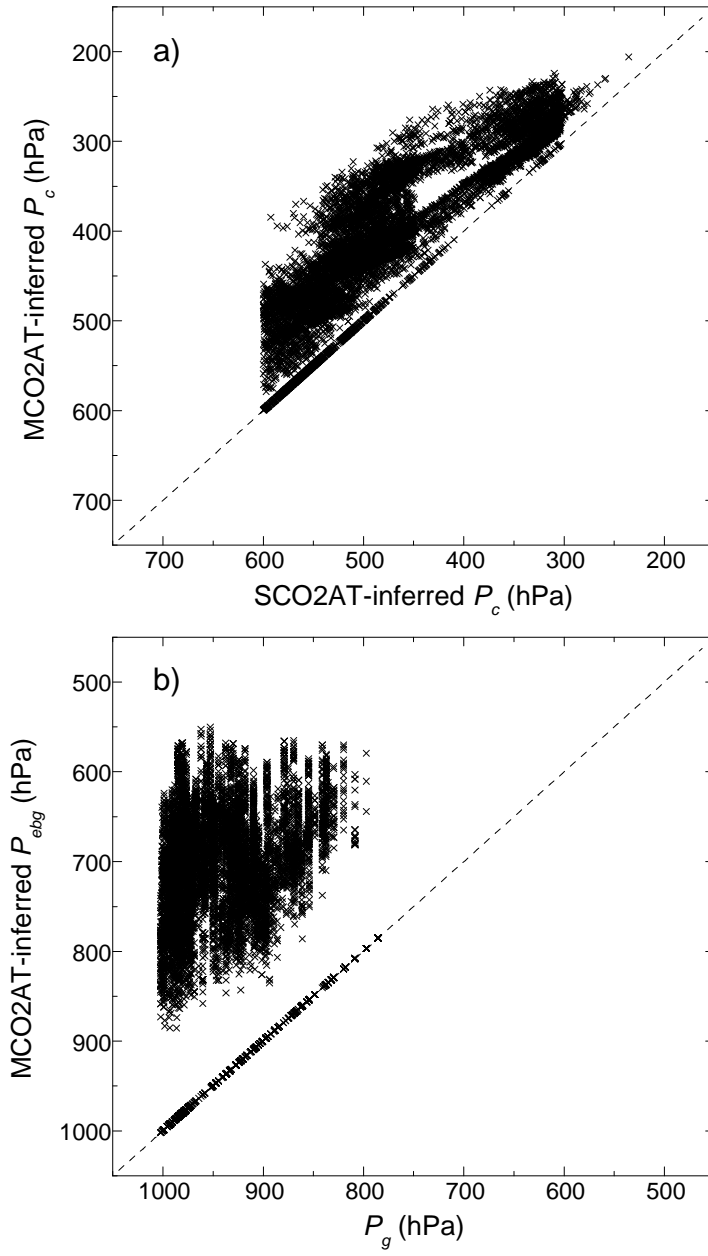
Fig. 5 Comparisons of a) MCO2AT-inferred P_c and SCO2AT-inferred P_c and b) MCO2AT-inferred P_{ebg} and P_g.

Fig. 6 GOES-12 imager-observed a) 13.3-μm and b) 10.7-μm brightness temperatures obtained on 24 May 2005 10:45 UTC for an area of 32°N-42°N and 105°W-91°W. Square near the center of the images marks the ARM SGP CART site.

Fig. 7 a) SCO2AT-inferred P_c, b) ground-level P_g, c) MCO2AT-inferred P_c, and d) MCO2AT-inferred P_{ebg}. Results are obtained for the GOES-12 imager data shown in Fig. 6.

Fig. 8 Vertical profiles of MMCR reflectivity (dBZ) at ARM SGP CART site, 24 May 2005. Red arrow indicates scan time of the GOES-12 imager data in Figs. 6 and 7.
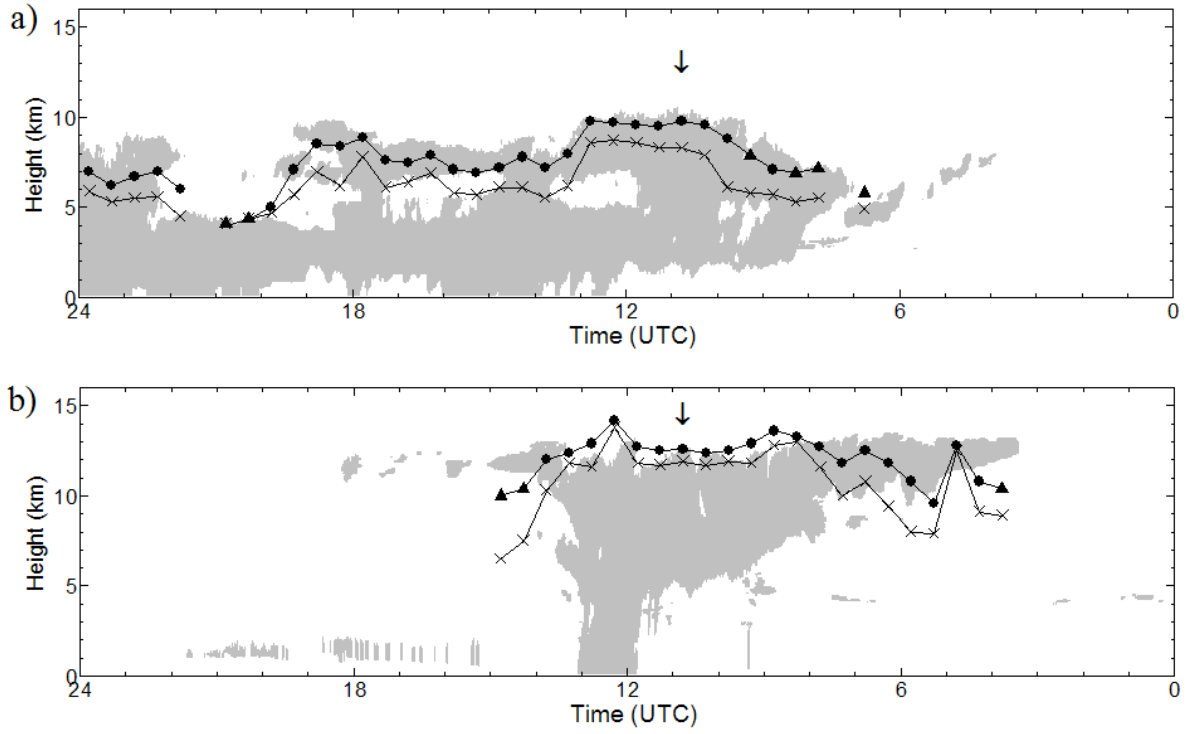
Fig. 9 MCO2AT-inferred CTHs (solid points) and SCO2AT-inferred CTHs (cross points) obtained on a) 1 May and b) 24 May 2005. Solid circles indicate overcast upper-cloud scenes and solid triangles indicate broken upper-cloud scenes. Grey areas are cloud masks constructed using the ARSCL data. Arrows indicate the time as shown in Figs. 4 and 8.
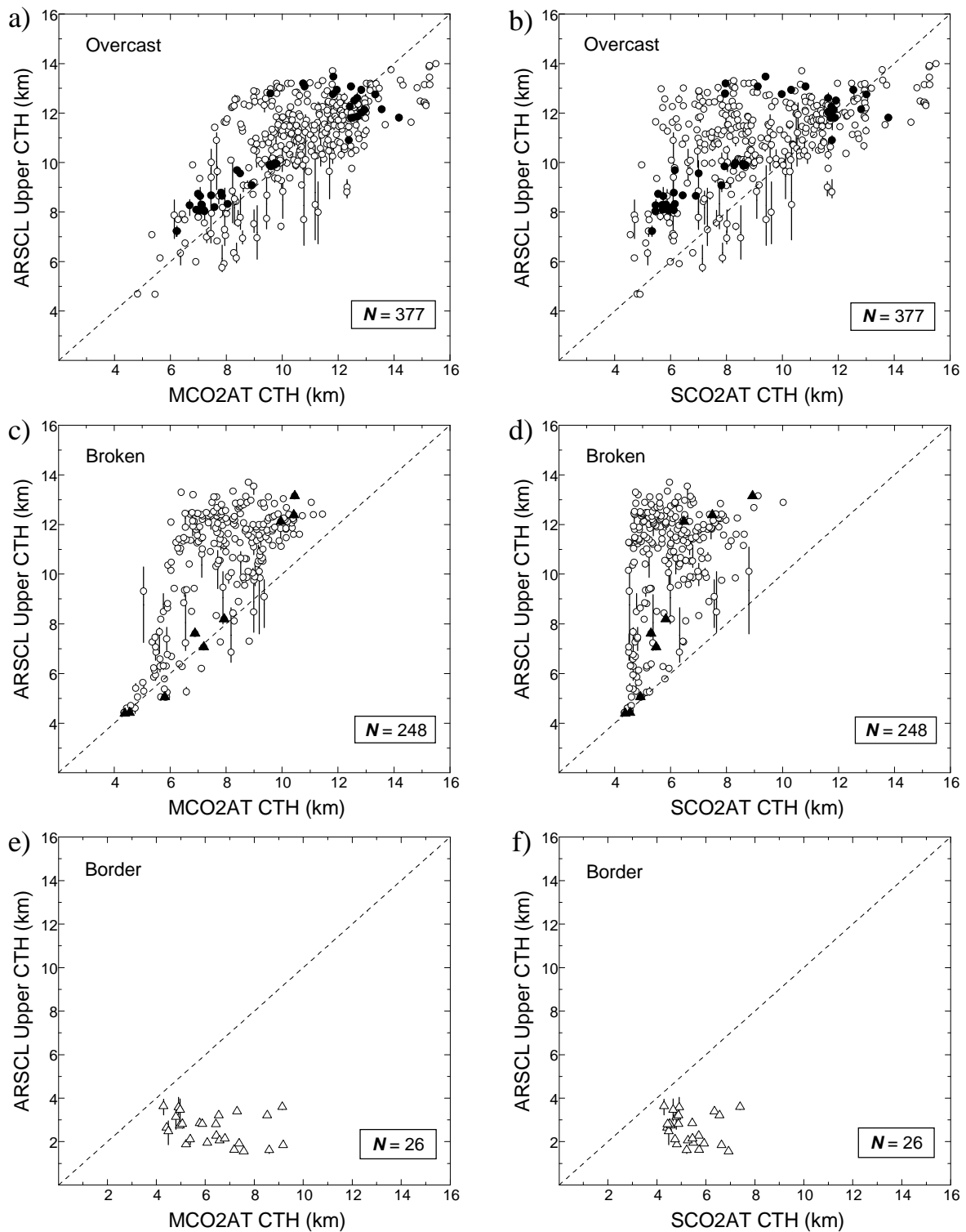
Fig. 10 Comparisons of ARSCL upper CTHs and the MCO2AT (a, c, e) and SCO2AT (b, d, f) inferred CTHs for overcast upper clouds (a, b), broken upper clouds (c, d), and border upper clouds (e, f). Vertical bar indicates the 25th-75th percentiles of the ARSCL data.
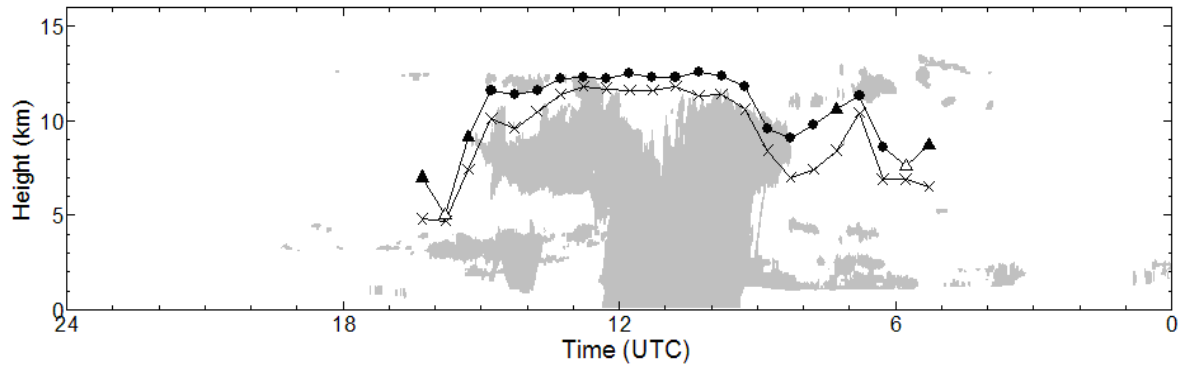
Fig. 11 CTH retrieved using MCO2AT (solid and open circles) and SCO2AT (crosses) for 26 May 2005. Solid circles indicate overcast upper-cloud scenes, solid triangles indicate broken upper-cloud scenes, and open triangles indicate border upper-cloud scenes. Grey areas are cloud masks constructed using the ARSCL data.
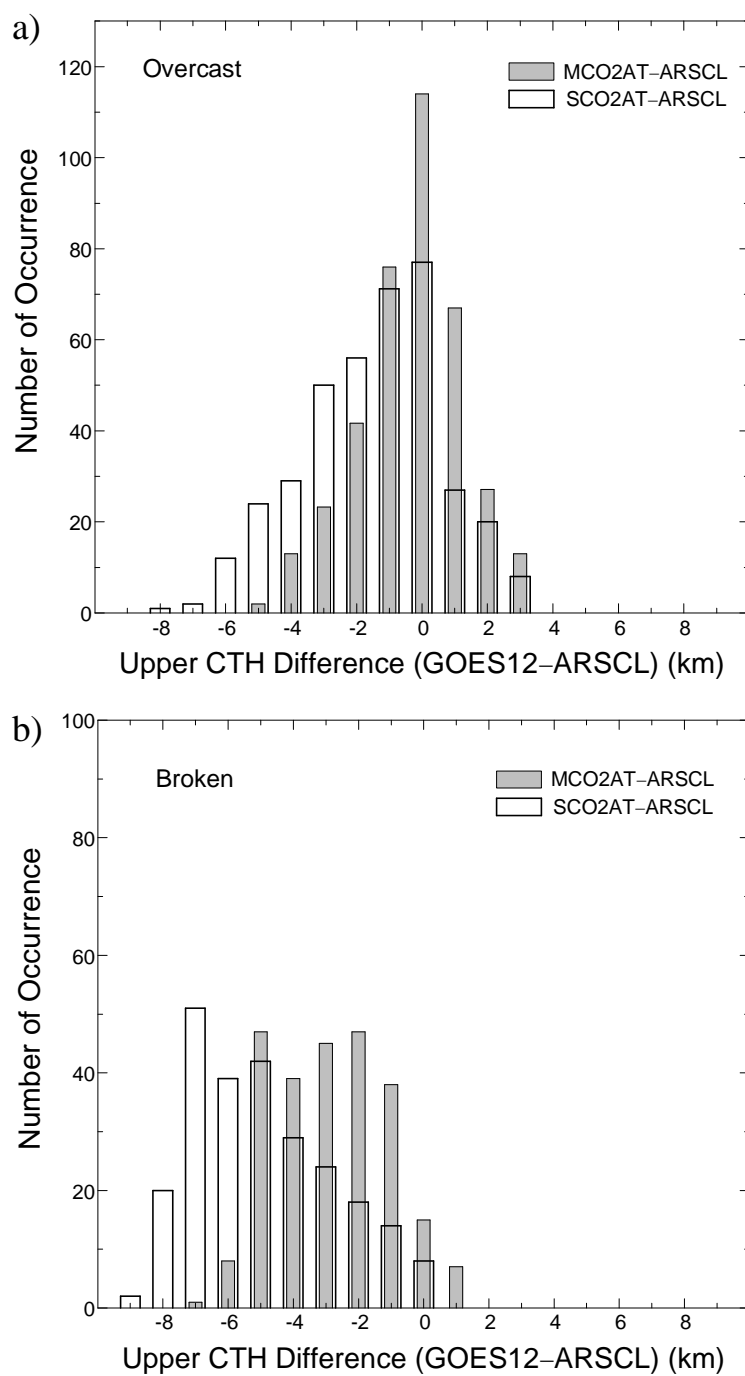
Fig. 12 Histograms of the upper CTH differences between MCO2AT minus ARSCL (filled grey) and SCO2AT minus ARSCL (no fill). a) for overcast upper-cloud scenes and b) for broken upper-cloud scenes.